# Measurement and Simulation of Thermal Distributions Across a Quantum Diamond Sensor With Nitrogen-Vacancy Centers

A Major Qualifying Project submitted to the faculty of
WORCESTER POLYTECHNIC INSTITUTE
in partial fulfillment of the requirements for
the degrees of Bachelor of Science in
Mechanical Engineering and Physics

by
Alexander Puhalski

Advised by
Professors Raisa Trubko and Pratap Rao


Worcester Polytechnic Institute
Worcester, MA, USA
May 6, 2022

# Abstract

A Quantum Diamond Microscope (QDM) is a device that is used to image magnetic fields and temperature distributions with nitrogen-vacancy (NV) centers in a diamond chip. Because the QDM uses a laser to excite the NV centers, there can be significant heating of the diamond chip along with the samples that are being measured. As a result, some samples of interest may become damaged; thus, it is important to characterize the temperature distribution across the NV diamond sensor. Through the use of Optically Detected Magnetic Resonance (ODMR) spectroscopy, thermal distributions across the diamond chip are measured, and the thermal effects of different imaging conditions are characterized. For typical operating conditions of 2.4 W of laser power and a 2.10 mm diameter Gaussian laser beam, the maximum temperature across the diamond sensor is 132 °C and the minimum temperature is 129 °C, and it takes about 4 minutes to reach thermal equilibrium. Thermal simulations are also conducted and experimentally verified in order to predict expected temperature distributions of the QDM. This work can serve as a starting point for developing methods to improve heat dissipation to be able to safely image samples that are sensitive to heat.

# Acknowledgements

First, I would like to thank my advisors Professor Raisa Trubko and Professor Pratap Rao for making it possible for me to do this project. Above all, I am especially thankful to Professor Raisa Trubko for her continuous support and mentorship and for allowing me to work in her lab. Without her, this project would not exist.

I would also like to thank graduate students Jacob Feinstein and Aidan Zlotak for their extensive help in the lab as well as fellow undergraduate students Camille McDonnell and Neil Kale for their support of this project.

# Contents

# List of Figures

# List of Tables

# 1. Introduction & Background

The Quantum Diamond Microscope (QDM) is a state-of-the-art device that takes advantage of the principles of quantum physics. By using nitrogen-vacancy (NV) centers in a diamond crystal, the QDM offers promising capabilities in the measurement and imaging of magnetic fields while also being able to perform measurements and imaging of temperature distributions. Unlike other magnetic field sensors such as the superconducting quantum interference device (SQUID) and magnetic force microscopy (MFM), the ensembles of NVs in diamonds utilized in QDMs provide reliable measurement capabilities at ambient temperatures and do not require special cooling [1]. QDMs can also be used at temperatures ranging from cryogenic to well over typical room temperatures. Importantly, the QDM offers a higher spatial resolution [1]. A QDM even has the ability to measure full-vector magnetic fields as well as the ability to measure slowly changing magnetic fields over time [2]. The extensive adaptability of the QDM setup allows for a broad range of applications across many different fields including studies of biological samples, geological samples, and electrical components among others [3, 4, 5].

Of particular interest to this project is the goal of being able to image the magnetic fields of biological samples, which often are sensitive to high temperatures and may become damaged after long exposure to these conditions. By taking advantage of the temperature measurement capabilities of QDMs, temperature information was gathered and analyzed to serve as a starting point for developing methods to improve the heat dissipation from these samples of interest.

## 1.1 The Quantum Diamond Microscope

A typical Quantum Diamond Microscope setup consists of several important components including an NV diamond sensor, Helmholtz coils or permanent magnets, a microscope objective, a camera, and a microwave loop. Two common QDM setups are shown below in Figure 1. While in both setups, a bias magnetic field is being generated, it is being done in two different ways. Setup A creates a bias magnetic field using two strong, permanent magnets, and setup B does this with Helmholtz coils oriented along the x, y, and z axes. A setup with Helmholtz coils similar to setup B is what is used in this work. The coils first cancel out the Earth's natural magnetic field and then also generate a bias magnetic field along one of the NV axes.

Other important parts of the QDM include a microscope objective and camera positioned above the NV diamond chip and sample in order to collect the fluorescence from the NV centers. Optical filters may also be used to help control what light is collected by the camera. A red-light filter is included in our setup to filter out all light with a wavelength below 650 nm. An excitation laser with a 532 nm wavelength is used to excite the NV centers while a microwave loop around the NV diamond chip is used to control the spin states of electrons in the NV centers.

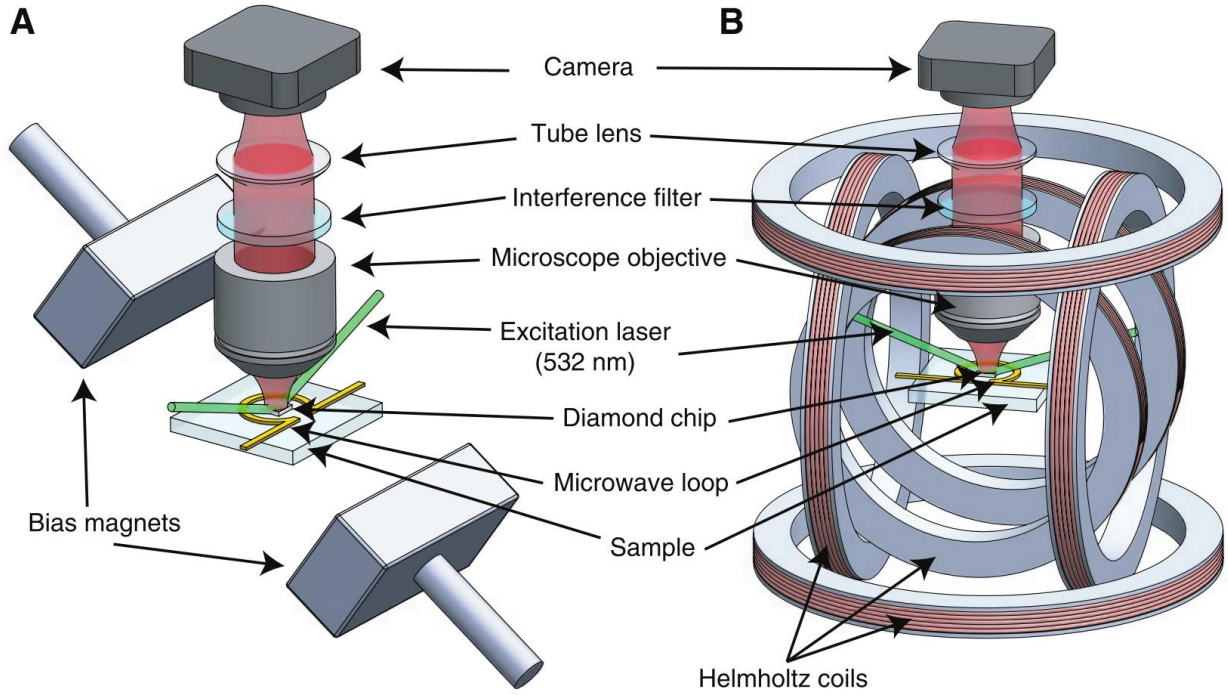


Figure 1: Quantum Diamond Microscope configurations with two permanent magnets (A) or Helmholtz coils (B) to create a bias magnetic field. An excitation laser is used to excite the NV centers in a diamond chip. Fluorescence from the NV centers is collected through a microscope objective by a camera. A microwave loop around the diamond is used to control spin states in the NV centers, and a sample is placed just below the diamond chip. Image from [2].

Together, these components of the QDM are used to perform Optically Detected Magnetic Resonance (ODMR) spectroscopy. Specifically, Continuous Wave Optically Detected Magnetic Resonance (CW ODMR) was used in all experiments described in this paper because it is a common method of magnetic imaging with a QDM and is the simplest to employ.

In a quantum diamond sensor with nitrogen-vacancy centers, electrons are excited from their ground state by the 532 nm laser as explained further in Section 1.2.1 and pictured in Figure 2. The amount of fluorescence that results from the decay back to the ground state is dependent on the spin states of the electrons in their ground state. Resonant microwave frequencies from the microwave loop can be used to flip the spin of the ground state electrons. By sweeping through a set of microwave frequencies and collecting the fluorescence from the NV centers, a spectrum can be generated like that pictured in Figure 3.

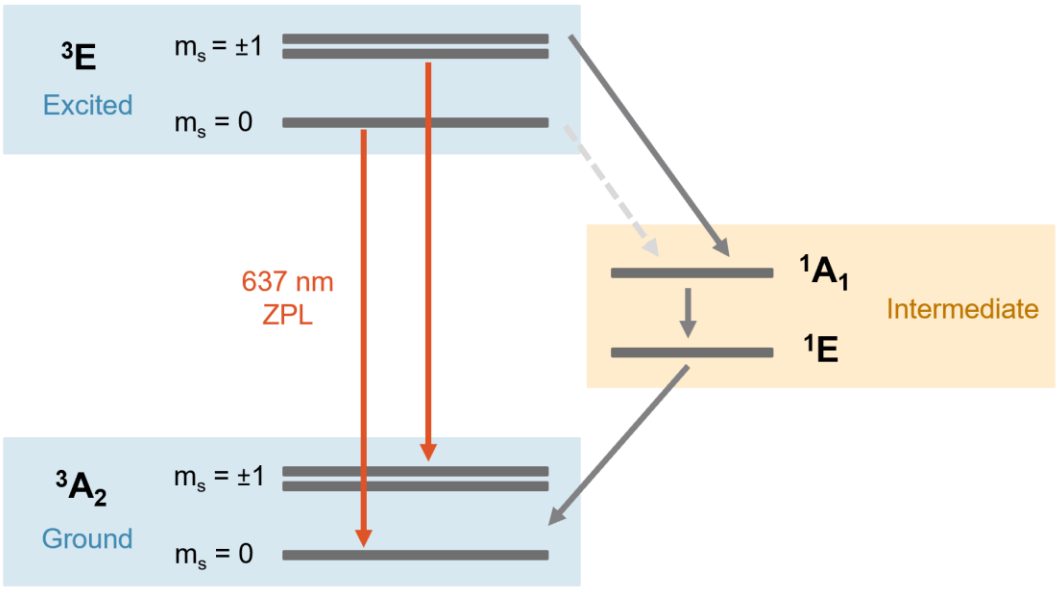


Figure 2: NV electron energy levels. The possible decay paths for electrons in the excited 3E state are shown with arrows. The radiative decay paths that result in red fluorescence are shown with red arrows. Non-radiative decay through the intermediate 1A1 and 1E levels is more likely for electrons in the $m_s = \pm 1$ state. Image from [5].

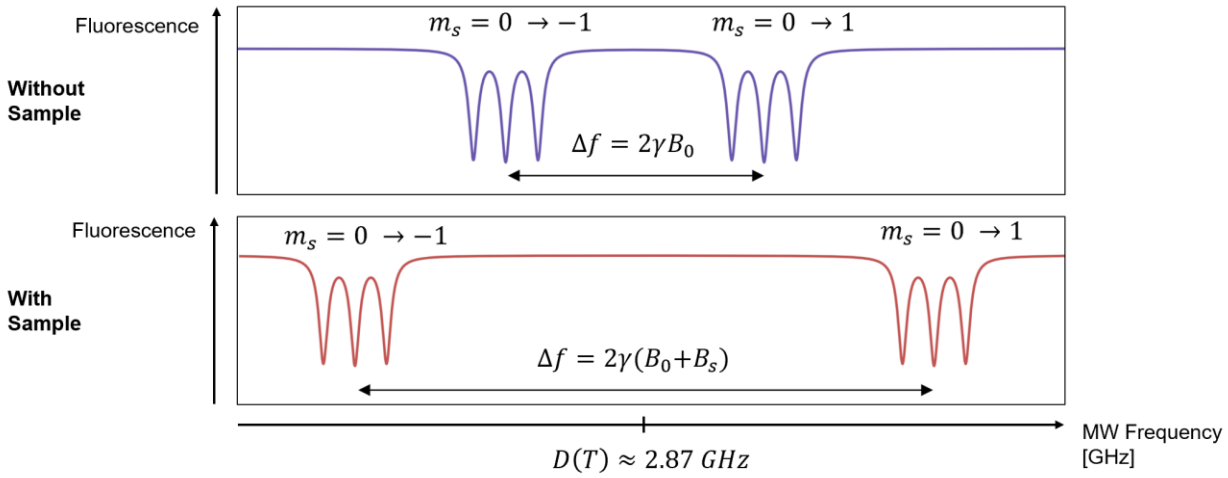


Figure 3: Sample ODMR Spectrum that would be obtained by a QDM. Two peaks with hyperfine structure are present representing the $m_s = 0 \rightarrow \pm 1$ transitions. When a sample with a magnetic field $B_s$ is present, a Zeeman shift $\Delta f$ proportional to the total magnetic field $B_0 + B_s$ occurs where $B_0$ is the bias magnetic field generated by the Helmholtz coils. Image from [5].

The ODMR spectrum shows NV fluorescence as a function of microwave frequency. By determining where the fluorescence decreases along the ODMR spectrum, the frequencies at which the spin states of the electrons in the NV centers change can be determined. The exact resonance

frequencies at which these spin state changes occur are dependent on both magnetic field strength and temperature; this allows for these two values to be calculated using the ODMR spectrum. Magnetic field strength is a function of the difference between the resonance frequencies whereas temperature is determined by examining the overall common shift of all resonance frequencies. The exact relation between these frequencies, magnetic field strength, and temperature is discussed further in Section 1.2.2.

## 1.2 Nitrogen-Vacancy Center Physics

Nitrogen-vacancy centers in diamond crystal structures are naturally occurring defects; however, these NV centers can also be intentionally created using techniques such as chemical vapor deposition (CVD) with nitrogen-doping to manufacture a diamond with a controlled concentration of NV centers. During the CVD process, thin layers of carbon atoms are deposited onto a substrate to gradually form a diamond crystal with the desired thickness. Throughout this process, nitrogen can be incorporated through nitrogen-doping as isolated-substitutional-nitrogen atoms in the crystal. These nitrogen substitution defects can then be converted to NV centers using irradiation and annealing techniques [6]. The diamond used in the experiments discussed in this paper is 4 mm x 4 mm x 1 mm in size. It was manufactured through chemical vapor deposition with a nitrogen-doping phase during the formation of the final layer in order to create a single layer of NV centers along one face of the crystal.

The geometry of an NV center can be described as a point defect in the crystal structure of a diamond (shown in Figure 4). It is a nearest-neighbor pair where a nitrogen atom has been substituted for one carbon atom and a neighboring point in the crystal lattice is left vacant. The free electrons that occupy this vacancy are the primary feature of the NV center that allow us to perform measurements using the QDM. Here, we specifically focus on the properties of negatively charged NV centers as these are the types of NVs used in these experiments. The free electrons of the NV consist of one electron each from the three carbon atoms adjacent to the vacancy, two additional electrons from the nitrogen atom, and one more electron from the lattice giving the NV its negative charge [2].

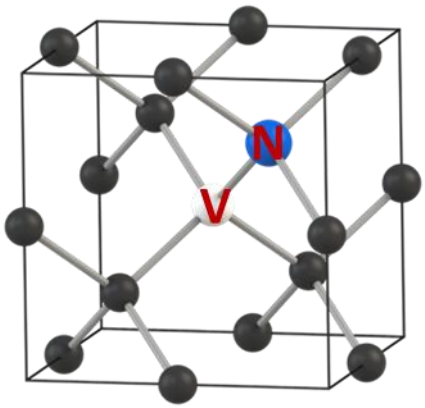


Figure 4: Nitrogen-vacancy center crystal structure. A Nitrogen atom (blue) has been substituted for a carbon atom (black), and a neighboring point in the lattice has been left vacant (white). The orientation of the NV defect can be along the (111), $(1\bar{1}\bar{1})$, $(\bar{1}1\bar{1})$, or $(\bar{1}\bar{1}1)$ axes. Here it is pictured in the (111) direction.

### 1.2.1 Nitrogen-Vacancy Center Electron Transitions

Quantum Diamond Microscopes use the fluorescence that results from the decay of NV centers' electrons to measure magnetic fields and temperatures. This is done by detecting changes to the ground state of the electrons that occupy the vacancies in the NVs. The ground state of these electrons is the spin triplet state $^3A_2$, shown in Figure 2 in Section 1.1. The corresponding excited state is the $^3E$ state with additional intermediate excited states $^1A_1$ and $E_3$, also pictured in the figure. Both the $^3A_2$ and $^3E$ states are composed of three fine structure states for $m_s = 0$, $m_s = -1$, and $m_s = +1$ which each additionally have their own three-level hyperfine structure (hyperfine structure is not shown in Figure 2) [2].

Using the 532 nm laser beam, the NVs are excited from the $^3A_2$ state to the $^3E$ state. The $^3A_2$ state and $^3E$ state are coupled together by a 637 nm zero-phonon line (ZPL), making the $^3E \rightarrow {}^3A_2$ transition a radiative transition where a red photon is emitted. [7]. This is the fluorescence that is captured by the camera in a QDM. In addition to the $^3E \rightarrow {}^3A_2$ decay path, an excited electron in the $^3E$ state may also follow the $^3E \rightarrow {}^1A_1 \rightarrow {}^1E \rightarrow {}^3A_2$ decay path. In this decay path, the $^3E \rightarrow {}^1A_1$ and $^1E \rightarrow {}^3A_2$ transitions are referred to as intersystem crossing (ISC) transitions. Decay through the $^3E \rightarrow {}^1A_1 \rightarrow {}^1E \rightarrow {}^3A_2$ path is non-radiative meaning no photon is emitted, unlike what occurs during the $^3E \rightarrow {}^3A_2$ transition. The probability of the $^3E \rightarrow {}^1A_1$ ISC transition occurring is only negligible for electrons in the $m_s = 0$ $^3E$ excited state. For electrons in the $m_s = \pm 1$ $^3E$ states, this $^3E \rightarrow {}^1A_1$ ISC transition has a non-negligible probability of occurring and resulting in a non-radiative decay [8]. This reduction in photon emission for NVs in the $m_s = \pm 1$ states due to the ISC decay path is large enough to be observed by the QDM during measurements. A quantitative value called contrast can be assigned to the change in fluorescence, defined as the percent difference in fluorescence between NV centers in the $m_s = \pm 1$ state and NV centers in the $m_s = 0$ state. For a single NV, the contrast be as high as 20%, but for measurements performed for this project using an ensemble of NVs, a typical contrast was 1.3-1.5% [2].

### 1.2.2 Nitrogen-Vacancy Center Hamiltonian

As mentioned in Section 1.1, the function of the microwave loop is to control the spin states of the electrons occupying the vacancies of the NV centers in order to carry out magnetic field and temperature measurements. The relation between these properties and the microwave frequencies that result in a spin flip can be accurately described by examining the following simplified Hamiltonian representing the energy of an electron in the $^3A_2$ ground state

$$\hat{\mathcal{H}} = hD(T)S_z^2 - \boldsymbol{\mu} \cdot \boldsymbol{B} \tag{1}$$

where $h$ is the Planck constant, $D(T)$ is the Zero Field Splitting (ZFS) frequency given as a function of temperature, $S_z$ is the dimensionless spin-1 matrix along the z-axis, $\boldsymbol{\mu}$ is the electron's magnetic moment, and $\boldsymbol{B}$ is the magnetic field at the electron [9]. The Hamiltonian can also be written using the spin vector $\boldsymbol{S} = (S_x, S_y, S_z)$ containing all three dimensionless spin-1 matrices, and the electron gyromagnetic ratio $\gamma$.

$$\hat{\mathcal{H}} = hD(T)S_z^2 - h\gamma(\boldsymbol{S} \cdot \boldsymbol{B}) \tag{2}$$

It is important to note here that the z-axis is assumed to be oriented along the axis of the nitrogen-vacancy defect. For ease of notation, it is generally assumed as being in the (111) direction according to the Miller Index used in crystallography to specify lattice planes and directions.

While the Hamiltonian described in Equations 1 and 2 is sufficient to describe an NV system for the purposes of measuring magnetic field strength and temperature, a complete Hamiltonian would include several additional terms. These additional terms include internal crystal stress in the diamond along with the interactions between the Nitrogen atom and the electrons as well as the effect of any present electric fields, but for our purposes these terms are negligible. The parts of the Hamiltonian included in Equations 1 and 2 are the Zeeman term because they can be used to describe the phenomenon of the Zeeman effect. The Zeeman effect is the shift in the resonance frequencies due to the introduction of a magnetic field. The bias magnetic field generated by the Helmholtz coils makes the Zeeman term dominant in the Hamiltonian and all other terms negligible. There is extensive documentation on the complete Hamiltonian for NV centers that will not be discussed in this work [2]. This simplified Hamiltonian leads to the equation giving the electron spin-flip probability as a function of microwave frequency, the shape of which can be graphically described as a Lorentzian curve [5].

$$\langle P_{0\to\pm1} \rangle = \frac{f_1^2}{(f - f_0')^2 + f_1^2} \tag{3}$$

Here, $f_1$ and $f_0'$ are dependent on both the static magnetic field and oscillating magnetic field strength and direction. The static magnetic field is the combination of the bias field generated by the Helmholtz coils and the magnetic field introduced by the sample being measured by the QDM; the oscillating magnetic field is generated by the microwave loop. The value $f_0'$ is of particular

interest as this is the resonance frequency for a spin-flip to occur. As $f$ approaches $f_0'$, the probability of a spin-flip occurring approaches 1. The exact value of $f_0'$ is given by

$$f_0' = D(T) \pm \gamma B_z \tag{4}$$

where the resonance frequency corresponding to the $m_s = 0$ to $m_s = -1$ spin-flip is represented by $D(T) - \gamma B_z$, and the $m_s = 0$ to $m_s = +1$ spin-flip is represented by $D(T) + \gamma B_z$. The magnetic field $B_z$ is the sum of the bias field generated by the Helmholtz coils ($B_0$) and the magnetic field from the sample being measured by the QDM ($B_s$) along the NV z-axis such that $B_z = B_0 + B_s$. The difference between these two resonance frequencies is $\Delta f = 2\gamma B_z = B_z \cdot 5.60\ MHz/G$ [5]. This relation between the difference of the resonance frequencies ($\Delta f$) and the total magnetic field ($B_z$) allows for the strength of the magnetic field from the sample of interest to be derived from the difference between resonance frequencies. By processing through a series of microwave frequencies surrounding the ZFS frequency, the resonance frequencies that induce transitions in NV centers from the $m_s = 0$ to the $m_s = \pm 1$ states can be found based on what frequencies result in reduced fluorescence. This is the principle that allows for the measurement of magnetic fields using a QDM.

For this work, we placed an emphasis on measuring temperature using a QDM. As previously mentioned, the ZFS frequency $D(T)$ is given as a function of temperature, implying that temperature can be derived from its relation to the resonance frequencies. To create a more complete equation for the resonance frequencies (Equation 4) by accounting for temperature, we can use the approximation $D \approx 2.87\ GHz$ at 300 K and its rate of change $dD/dT = \beta_T = -74.2\ kHz/K$ giving us the new equation [2, 10]

$$f_0' = D + \beta_T \delta_T \pm \gamma B_z \tag{5}$$

$$f_0' = 2.87\ [GHz] - \delta_T \cdot 74.2\ [kHz/K] \pm B_z \cdot 2.80\ [MHz/G]$$

where $\delta_T$ is the change in Temperature from 300 K. By finding the frequency given by $D + \beta_T \delta_T$ using the resonance frequencies, the temperature can be determined using the relation described by Equation 5.

## 1.3 Objectives

When taking measurements using a Quantum Diamond Microscope, some samples of interest may become damaged or have their properties altered due to the exposure to high temperatures that can result from them being in direct line of the laser beam. The goal of this project was to take advantage of the temperature measurement capabilities of QDMs in order to gain an understanding of the thermal distribution across the NV quantum diamond sensor under various conditions such as different laser powers and laser beam diameter. In doing so, we are able to use the resulting temperature information as a starting point for developing methods to improve

heat dissipation from the quantum diamond sensor so that samples that are heat sensitive, such as biological samples, may be imaged while experiencing fewer damaging conditions. The objectives for this project are the following:

1. To use the QDM to measure the temperature across the NV diamond sensor by creating a program that is able to calculate temperature measurements using the ODMR spectrum.
2. To utilize the newly created program for temperature measurement to characterize the time needed for the NV diamond sensor's temperature to reach equilibrium for various laser beam powers.
3. To study the effects that laser beam power and laser beam diameter size have on the temperature measurements collected by the QDM.
4. To utilize transient thermal analysis software to simulate the thermal distribution across the NV diamond sensor under the same conditions it experiences while being used in the QDM. This allows for the future testing of the thermal behavior of the NV diamond sensor under various experimental setups without the need for hours of data collection.

# 2. Temperature Measurements

In this chapter, we created a program to measure temperature using a QDM. We then used this program to perform experiments to determine the relation between laser power and temperature, to determine the amount of time required for the quantum diamond sensor to reach thermal equilibrium, and finally to examine the effect that laser beam diameter has on thermal distributions across the diamond.

## 2.1 Measuring Temperature Using a QDM

While QDMs are most commonly used to measure magnetic field strength, the properties of the NV centers in the quantum diamond sensor used by QDMs allow for the measurement of temperature as well, the physics of which was described in Section 1.2. As shown previously in Equation 5, a value for temperature can be calculated using the resonance frequencies measured via ODMR spectroscopy using the QDM. The QDM in our lab was already set up to image magnetic fields which also relies on knowing the resonance frequencies. The existing MATLAB program used for measuring magnetic field strength generates two arrays containing the resonance frequency values for measured for every pixel of the microscope camera. This is done by fitting three Lorentzian curves to the hyperfine structure of each resonance frequency on the ODMR spectrum collected for each pixel by the microscope camera. The result is one array of all the first resonance frequencies corresponding to the $m_s = 0$ to $m_s = -1$ transition and another array of all the second resonance frequencies corresponding to the $m_s = 0$ to $m_s = +1$ transition. To measure temperature using the QDM, it was advantageous to first run the raw data through the existing MATLAB program for magnetic fields and use the resulting resonance frequency arrays.

The next step was to create a MATLAB program for temperature measurement that could take the resonance frequency arrays and use them to calculate temperature values. To do this, we wrote the relation described by Equation 5 in a form that would give temperature as a function of the Zero Field Splitting frequency. Since the two resonance frequencies are equidistant from the ZFS frequency, the ZFS frequency can be described as the average of the resonance frequencies:

$$\bar{f} = \frac{f_2 - f_1}{2} \tag{6}$$

Here, $\bar{f}$ is the ZFS frequency and $f_1$ and $f_2$ are the first and second resonance frequencies respectively. Using this equation for the ZFS frequency and the relation described in equation 5, temperature as a function of the ZFS frequency can be written as

$$T(\bar{f}) = 300 - \frac{\bar{f} - D}{\beta_T} \times 10^6 = 300\ [K] - \frac{\bar{f} - 2.87\ [GHz]}{74.2\ [kHz/K]} \times 10^6 \tag{7}$$

By implementing Equation 7 into a MATLAB program that uses the two previously generated arrays of the resonance frequencies, values for temperature in Kelvin can be calculated at every pixel of the microscope camera. These values are then easily convertible from Kelvin to any desired unit of temperature measurement such as degrees Celsius. We used this MATLAB program to analyze the ODMR spectrums collected for the following experiments in this chapter to measure temperature.

## 2.2 QDM Temperature Measurement

In Section 2.2.1, we determined the relation between laser power and temperature using temperature measurements made with the QDM. Next, in Section 2.2.2, we carried out experiments to determine the amount of time required for the quantum diamond sensor in the QDM to reach thermal equilibrium. Finally, in Section 2.2.3, we used the QDM to measure the effect that laser beam diameter has on thermal distributions across the diamond.

### 2.2.1 Trends in Maximum Temperature Measurements

We carried out a study of the highest temperatures achieved at various laser powers first because understanding what the maximum expected temperature is for a given laser power is helpful when carrying out further experiments that are sensitive to high temperatures. To conduct this study, we repeatedly took measurements with no sample. We conducted measurements at different laser powers from lowest laser power to highest. This ensured that we did not take measurements with the NV diamond sensor starting at a temperature higher than what would otherwise be achieved at the specified laser power.

Prior to each measurement being carried out, we first set the laser power to the desired level and unblocked the beam so that it hit the diamond. We allowed this setup to sit without any interference for at least 45 minutes but up to 2 hours for the lower laser powers (i.e., 1.0 W and 1.5 W) prior to any data being collected. Doing so ensured that the diamond sensor was already completely heated and had reached a steady state. This is to say that any further change in temperature over time was negligible and the temperature of the system was able to be considered constant. We can make this assumption due to the consistently low heat capacity of diamond. The constant pressure heat capacity of diamond at 300 K is given as 6.57 J/mol·K as provided by the National Institute of Standards and Technology [11]. With a heat capacity this low, it is safe to assume that a diamond of this size will have fully finished heating prior to the 2-hour mark. This value is verified in Section 2.2.2 where the times required for the diamond to reach thermal equilibrium are examined in detail.

We took measurements for set laser powers in the range of 1.0 to 4.0 W at 0.5 W intervals (shown in Figure 5). Due to the fact that the beam passes through a beam splitter prior to it hitting the laser beam, there is a loss of power that occurs. Using a power meter from Thorlabs, we took measurements of the actual laser power after the beam splitter. We determined that the power is

reduced to approximately 80% of what it was set to. Therefore, if the laser power is set to 3.0 W of power, the actual laser power that is incident on the quantum diamond sensor is 2.4 $\pm$ 0.1 W. In this section and in following sections, the set laser powers being described are indicative of the value that the laser power was set to unless otherwise noted. For the range of 1.0 to 4.0 W at 0.5 W intervals, the actual laser power that was incident on the diamond was 0.8, 1.20, 1.6, 2.0, 2.4, 2.80, and 3.2 W. We collected each data set for a minimum of 6 hours but up to 10 hours to reduce noise in the data.

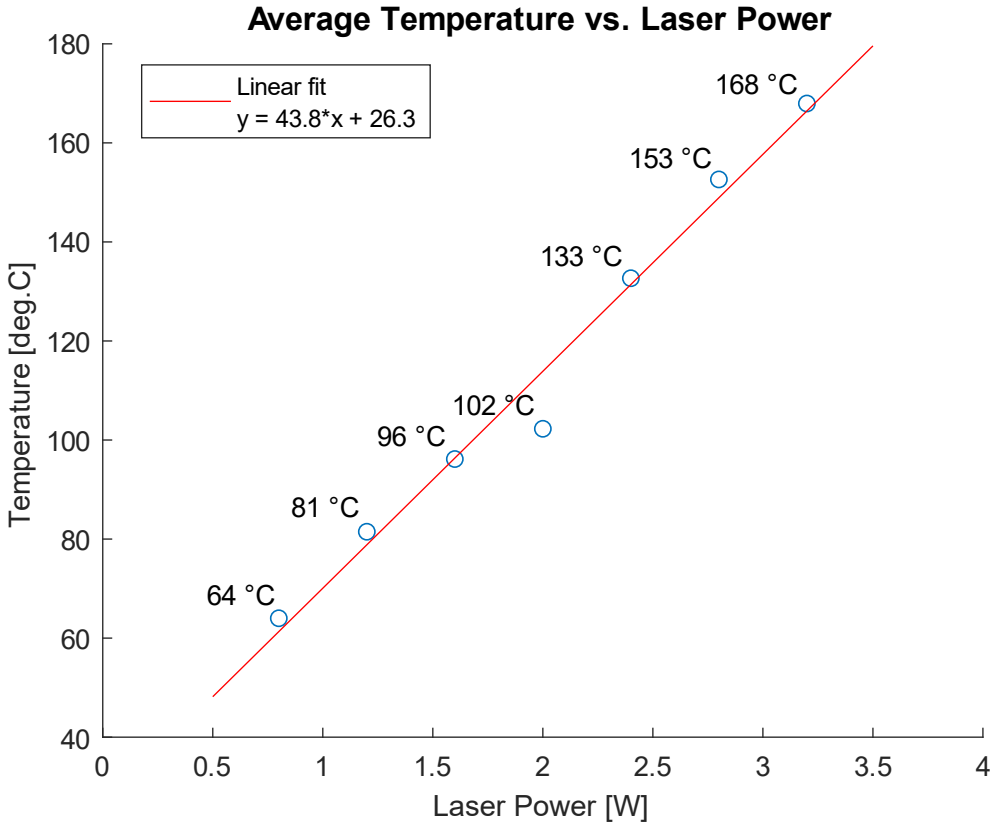


Figure 5: Average Temperature vs. Laser Power. The blue dots are the temperature measurements made using the QDM with the power from the laser that is incident on the diamond being 0.8, 1.20, 1.6, 2.0, 2.4, 2.80, and 3.2 W. Each dot is labeled with the exact temperature measured in degrees Celsius at each laser power. The red line is the trendline for the data with its equation displayed in the top left corner of the graph. The linear fit has an $R^2$ value of 0.981.

The average measured temperatures followed a linear pattern going from 64 °C measured at 0.8 W to 168 °C at 3.2 W. By performing a linear fit on the data, we found an equation for temperature as a function of the set laser power.

$$T(P) = 43.8 \cdot P + 26.3 \tag{8}$$

In Equation 8, $T$ is temperature in degrees Celsius and $P$ is the laser power in Watts. The value of $R^2$ for this fit is 0.981. This formula can be used to predict the average temperature that would be

reached during an experiment using a specific laser power. It could also be solved for laser power as a function of temperature and used to figure out a laser power to use to achieve a certain average temperature while measurements are being taken. If it is known that a sample of interest is not viable above a certain temperature, knowing how hot it would become during measurements is important to avoid damaging the sample.

As a way of verifying that the temperatures being measured by the QDM are reasonable, we used a thermocouple to determine a temperature range in which the measured temperatures at 0.8 W, 1.6 W, and 2.4 W would be expected to fall. A thermocouple is a device that can be used to measure temperature; it works by producing a temperature dependent voltage through two wires made of different metals. Two ends of the wires are soldered together and serve as the temperature measuring end. The other ends of the wires are attached to the voltage measuring system and kept at a reference temperature of 0 °C. The voltage is dependent on the difference in temperature between the hot end of the two connected wires and the cold end, so it is important to know what the cold reference temperature is. To measure the temperature dependent voltage, we used an Arduino UNO with an analog-to-digital converter (ADC) and coded a program in Arduino IDE to output temperature values.

In order to avoid directly touching the quantum diamond sensor with the soldered end of the thermocouple, we took two measurements to determine a temperature range within which the diamond's actual temperature would be expected to fall. After the diamond had reach its steady state temperature, we first placed the end of the thermocouple directly in the path of the laser beam above the diamond. Once the temperature there was measured, we touched the end of the thermocouple to the underside of the microscope slide that the diamond sits on directly underneath the diamond with the laser still on. These two measurements gave an upper and lower bound for the actual temperature of the diamond. For a laser power of 0.8 W, the thermocouple measurements gave a range of $57.5 \pm 3$ °C to $107.9 \pm 3$ °C. The QDM measured a temperature of 64 °C. For a laser power of 1.6 W, the thermocouple measurements gave a range of $60.2 \pm 3$ °C to $185.0 \pm 3$ °C. The QDM measured a temperature of 96 °C. For a laser power of 2.4 W, the thermocouple measurements gave a range of $65.0 \pm 3$ °C to $285.1 \pm 3$ °C. The QDM measured a temperature of 133 °C. The temperature ranges provided by the thermocouple are relatively large but can serve as a way of checking that the QDM measurements are not unreasonable. All of the temperatures measured by the QDM fall within the given ranges from the thermocouple, indicating that the QDM is providing reasonable measurements.

### 2.2.2 Temperature Equilibrium Time Measurements

Taking temperature or magnetic field measurements while the temperature of the diamond is still changing can impact the accuracy of the measurements. Understanding how long it takes for the quantum NV diamond sensor in the QDM to reach thermal equilibrium for different laser powers is important to ensure that the measurements taken are accurate. For the second objective of this project, we conducted a study to determine the time required for the quantum diamond sensor to reach thermal equilibrium for several different laser powers. To do this, we collected

data sets over multiple intervals of time for each laser power, starting with shorter data collection times as low as 4 minutes and progressing to time intervals as long as 1.5 hours.

We performed experiments for set laser powers of 1.0 W, 2.0 W, 3.0 W, and 4.0 W. As explained in Section 2.2.1, the actual power that was incident on the diamond for these experiments would have been 0.8 W, 1.6 W, 2.4 W, and 3.2 W respectively. Prior to each experiment, we allowed the quantum diamond sensor to cool overnight from previous measurements to ensure that we observe the entire heating process during measurements. At the start of each experiment, we set the laser beam to the desired power level and started a timer as soon as the beam was unblocked so that it directly hit the diamond. We set the number of sweeps through the microwave frequencies to the desired amount corresponding to how long data would be collected. We recorded the time on the timer the moment data collection started; the experiment was monitored closely so that the time could be recorded again as soon as data collection ended. We then adjusted the number of sweeps and repeated the process until it could be assured that the diamond had reached equilibrium and that we had collected enough data to accurately represent the heating process. These periods of data collection for a single laser power ranged from 2 hours and 45 minutes up to 7 hours and 15 minutes.

Following all data sets being collected for a single laser power and all timestamps being recorded, all sets of data were processed through the MATLAB code described in Section 2.1 to calculate the average temperature of the quantum diamond sensor during each data collection period. Next, we took the corresponding time value for each of these average temperature values to be the median of the time over which the data for that temperature was taken. For example, if data collection was started at 120 minutes and ended at 133 minutes, the corresponding time value for the average temperature calculated from that data would be 117.5 minutes.

We then plotted these temperature values in MATLAB and performed a fit using the custom curve fitting equation:

$$T(t) = a - b \cdot e^{-c \cdot t} \tag{9}$$

where $T(t)$ is the average temperature of the diamond in degrees Celsius, $t$ is the time that the laser has been hitting the diamond in minutes, and $a$, $b$, and $c$ are the fit parameters used to generate a fit equation for the heating of the quantum diamond sensor for each laser power. Figure 6 shows the resulting curve fits for each laser power that data was collected for.

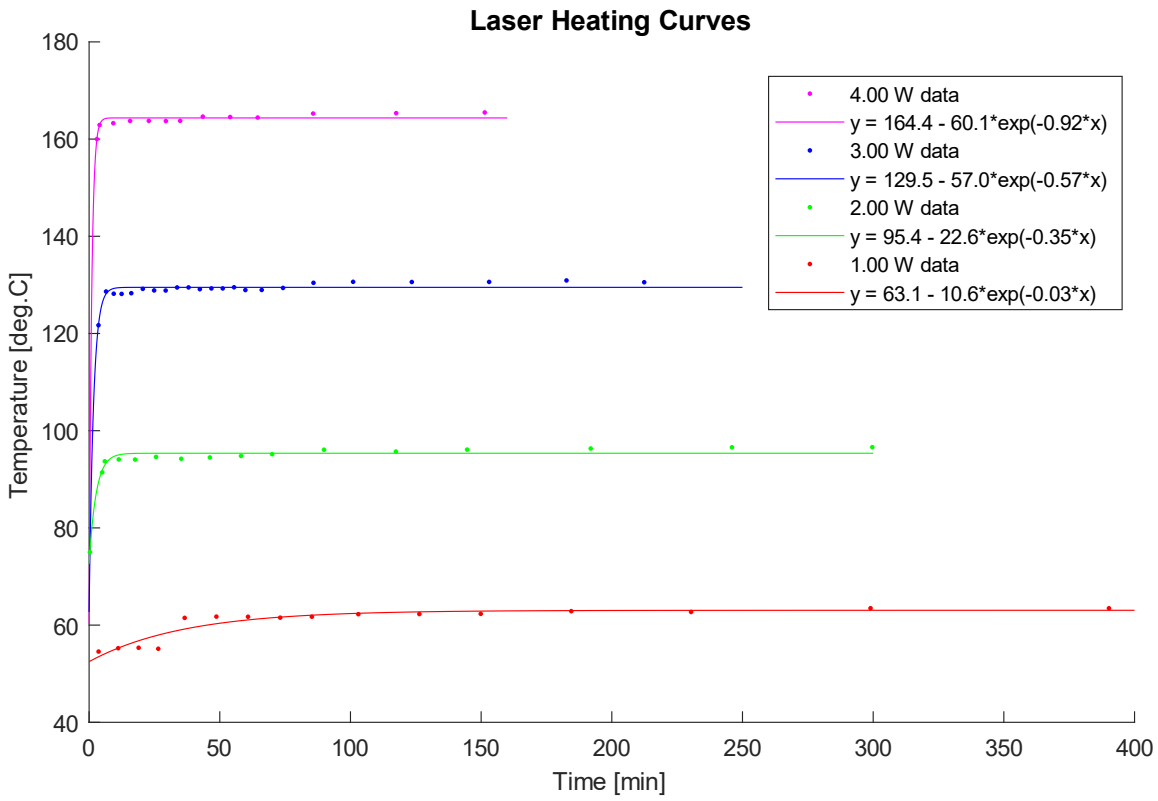


Figure 6: Temperature vs. time that laser has been incident on the quantum diamond sensor for 1.0 W (red), 2.0 W (green), 3.0 W (blue), and 4.0 W (pink). The temperature measurements at specific times are indicated with dots. A line showing the fit for the heating curve is included for each set laser power with the specific equation written in the box in the top right.

Based on the fits made using Equation 9, the final steady state temperatures for set laser powers of 1.0 W, 2.0 W, 3.0 W, and 4.0 W are 63.05 °C, 95.37 °C, 129.50 °C, and 164.40 °C respectively. These values for the maximum temperature reached at each laser power are all 0.79 °C to 3.55 °C lower than the values measured in Section 2.2.1. This is due to the nature of the fit made using Equation 9 where its maximum value ($a$) is drawn lower by the prior temperature points measured during the heating period. The more accurate values for the steady state temperature are those measured in Section 2.2.1 since they do not rely on a fit that is generated using measurements made during the heating process. The fit generated in this section is primarily helpful in determining the time required for the diamond to reach thermal equilibrium.

From these experiments we can conclude that the amount of time that the quantum diamond sensor needs to be exposed to the laser beam before it reaches its maximum temperature decreases rapidly as laser power is increased. Using the fitted heating curves to determine the amount of time necessary for the diamond to reach 99% of its maximum temperature relative to room temperature gives 116.96 minutes, 9.83 minutes, 6.98 minutes, and 4.05 minutes for set laser powers of 1.0 W, 2.0 W, 3.0 W, and 4.0 W respectively. While it would have been beneficial to gather more data points closer to the start of the heating process, especially for 3.0 W and 4.0 W of set laser power,

temperature measurements with a QDM at these laser powers requires at least 3-4 minutes of data collection to obtain useable data. This is a potential limitation of using a QDM to measure temperature. However, due to the fact that even taking only 3-4 minutes of data at these highest laser powers yields temperatures already approaching thermal equilibrium, we can be confident that the majority of the heating would have occurred during these initial 3-4 minutes. Table 1 shows the times needed for the quantum diamond sensor to reach 95% and 99% thermal equilibrium relative to room temperature at 1.0 W to 4.0 W of set laser power.

| Set Laser Power [W] | Incident Laser Power [W] | Time to 95% Thermal Equilibrium [min] | Time to 99% Thermal Equilibrium [min] |
|---|---|---|---|
| 1.0 | 0.8 | 58.50 | 116.96 |
| 2.0 | 1.6 | 5.19 | 9.83 |
| 3.0 | 2.4 | 4.12 | 6.94 |
| 4.0 | 3.2 | 2.31 | 4.05 |

Table 1: Time before the quantum diamond sensor reaches 95% and 99% of the temperature for thermal equilibrium relative to the room temperature at 1.0 W to 4.0 W of laser power

Despite only having 4 data points each, both of these measurements of the time it takes for the diamond to reach a percentage of its thermal equilibrium appear to adhere to a power function. Figure 7 shows the values from Table 1 with two approximate power functions fit to the data.

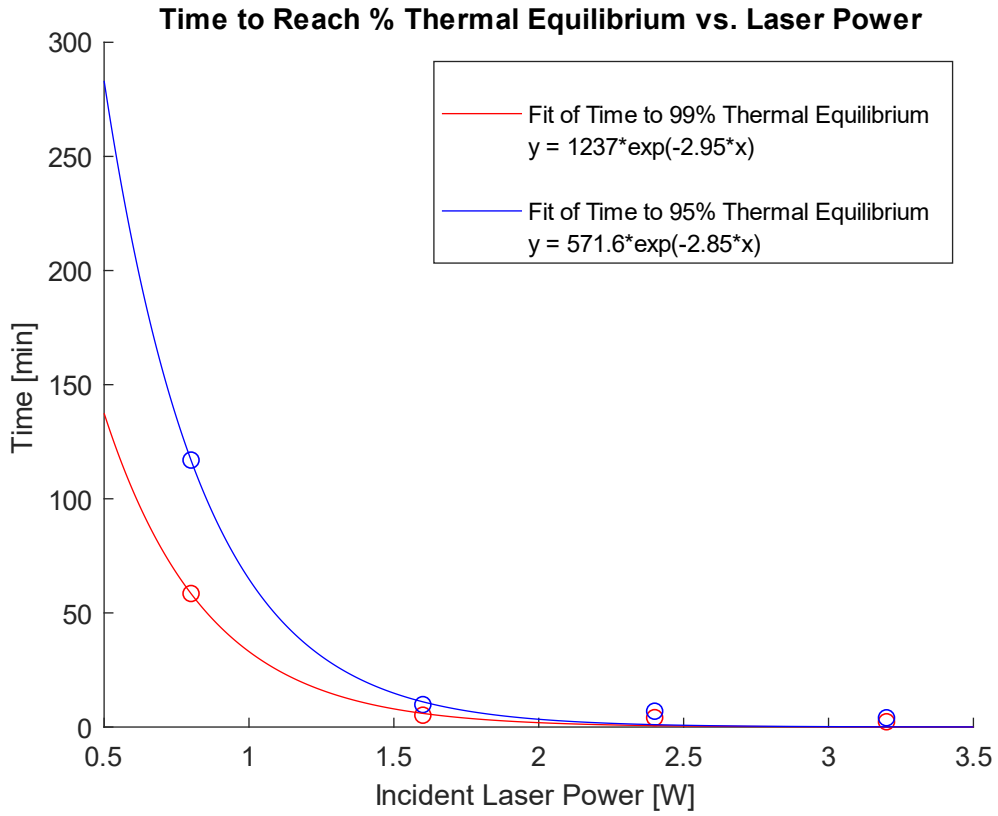


Figure 7: Time to Reach 99% (blue) and 95% (red) Thermal Equilibrium Relative to Room Temperature vs. Laser Power.

Based on both of these trends, it can be conjectured that the time it takes for the quantum diamond sensor to reach thermal equilibrium approximately follows the proportionality relation

$$t_E \propto \frac{1}{P^3} \tag{10}$$

where $t_E$ is the time from the start of heating by the laser needed for the diamond to reach thermal equilibrium, and $P$ is power in Watts of the laser. While more experiments would be necessary to verify this relation shown in Equation 10, it is still conducive to providing insight into the thermal behavior to expect at different laser powers. If it is necessary to use a 1.0 W of laser power for an experiment in order to not damage a sample being measured, the quantum diamond sensor should first be allowed to heat for up to 2 hours so that it reaches thermal equilibrium. If a lower laser power is not necessary, or if it is desired to start taking measurements quickly, it may not be necessary to wait more than 4 minutes while using 4.0 W of set laser power to be sure that the diamond has reached its thermal equilibrium. Due to the time-consuming nature of these particular experiments, we were only able to conduct these experiments at the integer power levels. In future work, it would be suggested to conduct further experiments so as to be able to compare the heating of more laser power levels.

### 2.2.3 Effect of Laser Beam Size

The third objective involved studying the effects that laser beam diameter has on the temperature distribution across the NV diamond sensor. To complete this objective, we used a system of two consecutive convex lenses with different focal lengths to adjust the beam diameter. An optical image of the diamond was then taken and saved. After being processed through MATLAB, we determined the laser beam diameter using the image. The optical images of the diamond are shown in the left column of Figure 8. The colors in the optical images are not representative of the actual colors in the image. Instead, these colors are used to show relative brightness. Since the laser beam in the QDM hits the diamond at an angle, the profile of the area where the beam is incident on the diamond is not circular but elliptical. Let all mentions of the diameter or radius of the beam be assumed as referring to the larger diameter or radius of the elliptical profile. Based on the angle of incidence, the smaller diameter/radius of the elliptical profile is 92.22% of the larger diameter/radius.

For each new adjusted beam size, we took data using the QDM to create a thermal distribution map. For each experiment, we took data for 6 hours. The laser was kept at a set power of 3.0 W so that the resulting thermal maps could be compared with one another. The actual laser power that is incident on the quantum diamond sensor is $2.4 \pm 0.1$ W due to the loss of power from the beam splitter as described in Section 2.2.1. Understanding the actual power incident on the diamond is especially important when it comes to simulating these experiments (Chapter 3). Figure 8 shows the resulting thermal distributions across a 1.90 mm x 1.45 mm section of the quantum diamond sensor for laser beam diameters of 0.90 mm, 1.73 mm, and 2.10 mm.

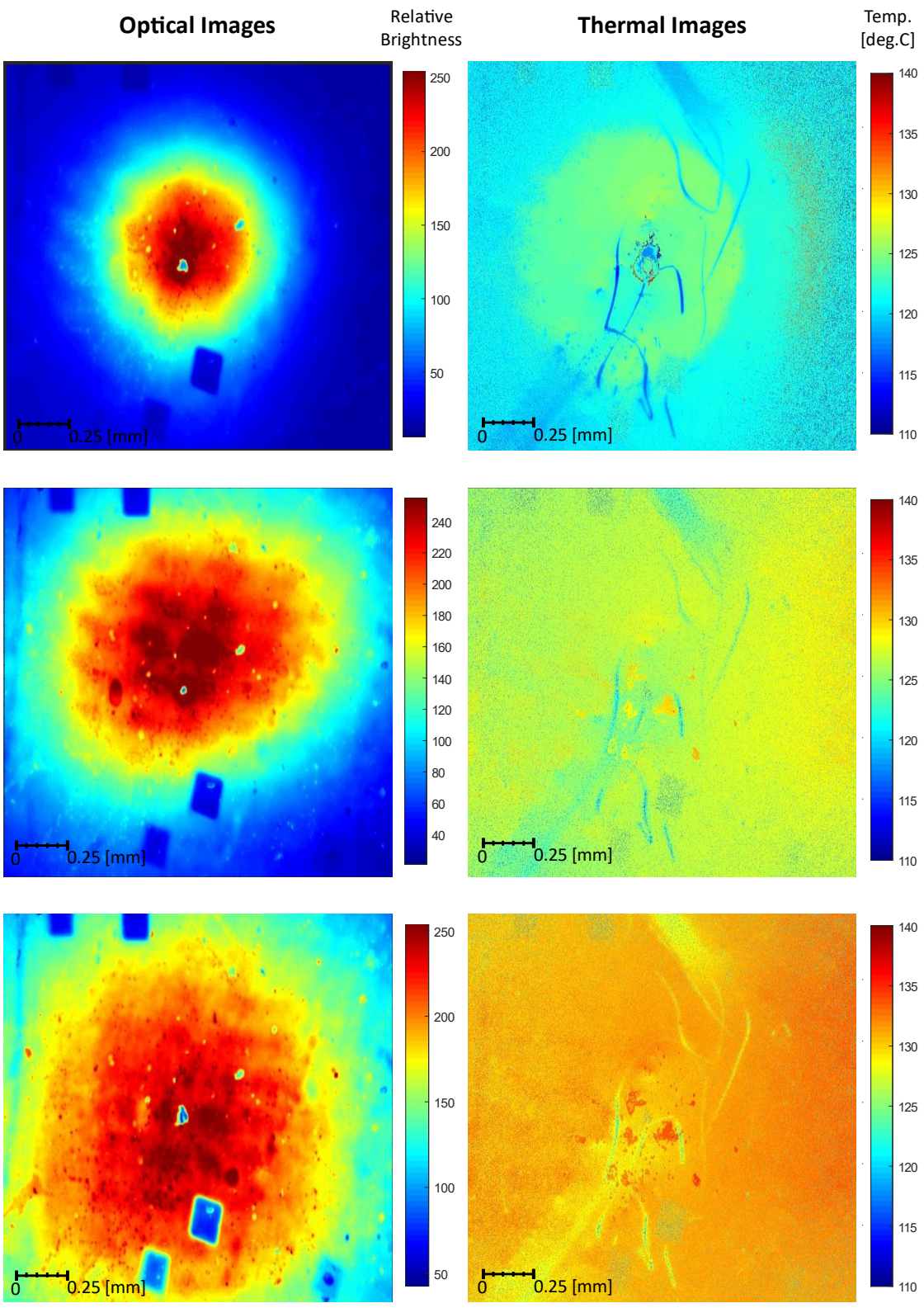


Figure 8: Optical images of a laser beam on a quantum diamond sensor (left) and corresponding thermal maps of the quantum diamond sensor (right). We used laser beam diameters of 0.90 mm

(top row), 1.73 mm (middle row), and 2.10 mm (bottom row) in these experiments all at 2.4 W of power incident on the diamond.

The maximum temperature for the 0.90 mm diameter laser beam is approximately 126 °C and the minimum temperature is approximately 121 °C. For the 1.73 mm diameter laser beam, the maximum temperature is approximately 128 °C and the lowest temperature is approximately 125 °C. For the 2.10 mm diameter laser beam, the maximum temperature is approximately 132 °C and the lowest temperature is approximately 129 °C. Based on these thermal maps, several conclusions can be drawn:

1. The maximum measured temperature increases as the laser beam diameter increases. From the smallest beam diameter to the largest, there was a 166.7% increase in beam diameter with a 3.2% increase in maximum measured temperature.
2. The range of temperatures across the diamond is larger for smaller laser beam diameters. With the 0.90 mm beam diameter, there was a difference of approximately 5 °C between the region where the beam was hitting the diamond and the region where it was not. For both the 1.73 mm and 2.10 mm beam diameters, there was a difference of approximately 3 °C between the highest and lowest temperatures measured.
3. The temperature gradient across the diamond is more evenly distributed for larger laser beam diameters. For the 0.90 mm beam diameter, temperatures across the diamond were primarily at either the highest (126 °C) or lowest (121 °C) temperatures measured with very little in between. For the two larger laser beam diameters of 1.73 mm and 2.10 mm, there was a more even distribution of temperatures with the majority of points being between the highest and lowest temperature values.

# 3. Simulations

For the fourth objective of this project, we simulated the thermal distribution across the quantum diamond sensor using SOLIDWORKS Transient Thermal Analysis software. We replicated experimental setups of the quantum diamond sensor described in Chapter 2 using this software and compared the results from the simulations with the experimental results. Performing these simulations served two primary roles:

1. To develop a method for simulating the quantum diamond sensor that provides a reasonable approximation of the actual experiment and can be verified using actual measurements taken using the QDM.
2. To be able to use this method for simulating the quantum diamond sensor under new experimental setups so as to provide insight into what we can expect the thermal behavior of the system to be without needed to take data with the QDM.

The following sections describe the methods used to perform these simulations and the results.

## 3.1 Simulating Temperature of a Diamond Illuminated with a Gaussian Laser Beam

In Section 3.1.1, we determined the material properties of diamond and assigned them to a SOLIDWORKS model of the quantum diamond sensor used in the QDM. In Section 3.1.2, we applied a method of simulating a laser beam with a Gaussian irradiance profile to the model in a SOLIDWORKS Transient Thermal Analysis simulation. Finally, in Section 3.1.3, we determined the remaining thermal boundary conditions and initial conditions for the diamond and assigned them in the simulation.

### 3.1.1 Material Properties of Diamond

The first step to simulate the quantum diamond sensor was to create a 4 mm x 4 mm x 1mm rectangular prism in SOLIDWORKS and assign the correct material properties of diamond to it (these are the dimensions of the quantum diamond sensor used in all experiments as first stated in Section 1.2). A fully accurate representation of the quantum diamond sensor would not be a perfectly smooth diamond. There would be minor surface defects across all faces of the diamond that cannot be consistently recreated in a SOLIDWORKS model. These minor defects to not have a significant impact on the thermal loads or boundary conditions experienced by the diamond, so it is assumed that these imperfections do not have a significant impact on the accuracy of the thermal simulations being performed. Performing simulations with a diamond that has perfectly smooth faces still provides accurate results that are comparable to the real quantum diamond sensor, as is shown in the results in Section 3.2.

Due to the SOLIDWORKS material library not having diamond as a default material in its database, it was necessary to create a custom material in the library and manually assign all material properties. For this project, we took the material properties of diamond from the Ansys Fluent 2021 R2 material library since diamond is included in that software's built-in database. We assigned these values to a new custom material in the SOLIDWORKS material library under the name "diamond". A complete list of the values assigned for all material properties is shown below in Table 2:

| Property | Value | Unit |
|---|---|---|
| Elastic Modulus | 1.1272e+12 | N/mm^2 |
| Poisson's Ratio | 0.2 | N/A |
| Shear Modulus | 450000 | N/mm^2 |
| Mass Density | 3509.3 | Kg/m^3 |
| Tensile Strength | 1200 | N/mm^2 |
| Compressive Strength | 110000 | N/mm^2 |
| Yield Strength | 140000 | N/mm^2 |
| Thermal Expansion Coefficient | 1.0496e-06 | /K |
| Thermal Conductivity | 1445 | W/(m·K) |
| Specific Heat | 528.95 | J/(kg·K) |

Table 2: Material Properties of Diamond [12]

### 3.1.2 Simulating a Gaussian Beam

The 532 nm laser used in the QDM has a Gaussian irradiance profile. This means that the amount of laser power that the laser is outputting over an area is not uniform but instead follows a Gaussian distribution as shown in Figure 9. In order to emulate a Gaussian irradiance profile using a SOLIDWORKS Transient Thermal Analysis simulation, we used an estimation for the distribution of laser power. We can do this by breaking up the area where the laser beam is hitting the diamond into concentric rings and assigning the amount of power generation in that area to be proportional to the area under the corresponding section of a Gaussian curve in Equation 11. First, a gaussian curve must be fitted to the desired radius of the beam. It is accepted that the radius of a Gaussian beam can be defined as the point where the relative intensity of the beam is $1/e^2$ or approximately 13.5% of the maximum intensity [13]. This point corresponds to two standard deviations or $r = 2\sigma$. This means that to simulate a beam with a given diameter, the necessary standard deviation for the corresponding Gaussian curve is one quarter of the diameter. (As mentioned in Section 2.2.3, all mentions of diameter and radius are in reference to the larger diameter/radius of the elliptical beam profile incident on the diamond surface.)

$$g(x) = \frac{1}{\sigma\sqrt{2\pi}} e^{-\left(\frac{x^2}{2\sigma^2}\right)} \tag{11}$$

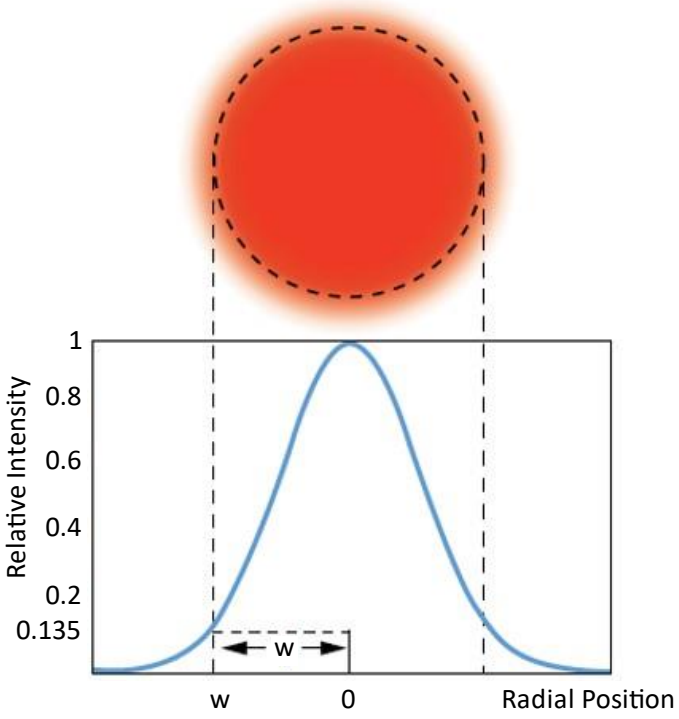


Figure 9: Irradiance Profile of a Gaussian beam. The waist of the beam is defined as the point where the relative intensity is 1/e^2 (~13.5%) of the maximum intensity. This value ($w$) is the radius of the beam. Image from [13].

Next, we can break down the area where the Gaussian beam is incident on the diamond into concentric elliptical rings at intervals defined as a fraction of the standard deviation. The reason for choosing to use elliptical rings instead of circular rings is explained in Section 2.2.3. Breaking the area under the beam into concentric elliptical rings allows for the defined radius of the beam ($2\sigma$) to be broken up into an integer number of parts. We can define the width of each ring as the outer radius minus the inner radius. For these simulations, we used a width of one half of a standard deviation such that $r_o - r_i = 0.5\sigma$. Let $r_o$ and $r_i$ be the outer and inner radius respectively. By making the divisions smaller, the simulation of the Gaussian distribution becomes more accurate. The most accurate ring width for simulating the Gaussian distribution would be represented as

$$r_o - r_i = \lim_{n\to\infty} \frac{1}{n}\sigma \tag{12}$$

Figure 10 shows the distribution of the Gaussian beam in each subdivision of the elliptical region.

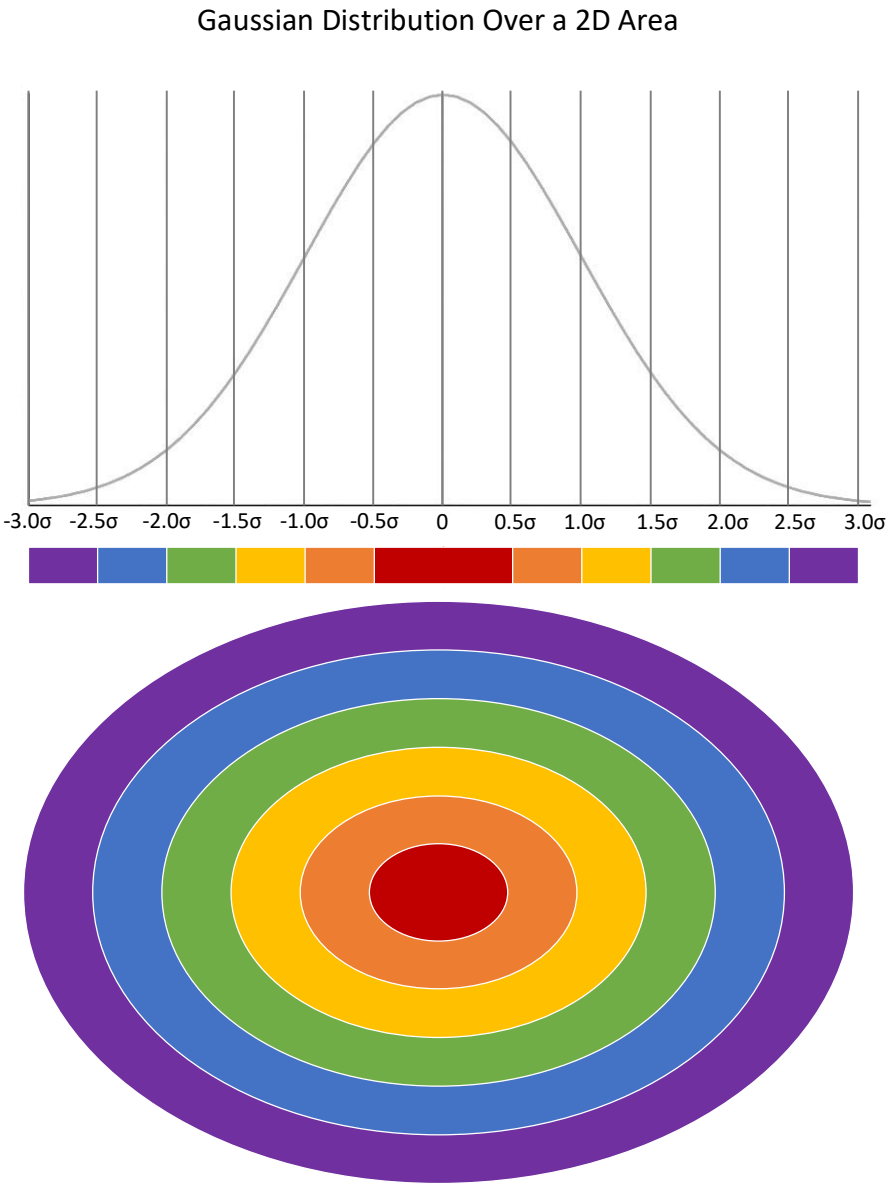


Figure 10: Distribution of a Gaussian beam over an elliptical region. The elliptical region is broken down into concentric elliptical rings each with a width of $0.5\sigma$. The center of the elliptical region is shown in red and corresponds to the center of the Gaussian distribution with an inner radius of $0$ and an outer radius of $0.5\sigma$. The outer ring of the elliptical region is shown in purple and corresponds to the outer rang of the Gaussian distribution with and inner radius of $2.5\sigma$ and an outer radius of $3.0\sigma$. The total radius of the elliptical region is $3.0\sigma$.

The percentage of the laser power in each ring is equal to the area under the Gaussian curve that is over that region. While the accepted definition for the radius of the Gaussian beam is $2\sigma$, the actual distribution of the laser power covers a larger area. By simulating the Gaussian beam over an elliptical area with a radius of $3\sigma$, 99.73% of the total laser power is accounted for. This

means that for a simulation for a beam with 2.4 W of power, approximately 2.39 W of power would be accounted for in the simulation. This means that the simulated temperatures may be slightly lower than the actual measured temperatures due to the 0.01 W reduction in power.

| Inner Radius | Outer Radius | Percent of Gaussian Curve Over this Region | Laser Power in this Region for 2.4 W Total Power |
|---|---|---|---|
| 0 | 0.5 σ | 38.29 % | 0.9190 W |
| 0.5 σ | 1.0 σ | 29.98 % | 0.7195 W |
| 1.0 σ | 1.5 σ | 18.36 % | 0.4406 W |
| 1.5 σ | 2.0 σ | 08.82 % | 0.2117 W |
| 2.0 σ | 2.5 σ | 03.30 % | 0.0792 W |
| 2.5 σ | 3.0 σ | 00.98 % | 0.0235 W |

Table 3: Distribution of laser power for concentric regions of the area under the laser beam with $0.5\sigma$ width

Table 3 shows the distribution of laser power in each region of the elliptical beam profile. In the SOLIDWORKS simulation, we created a sketch of these six concentric elliptical regions (like that pictured in Figure 10) with the appropriate dimensions based on the desired beam diameter. We ran all simulations for the different beam sizes using 2.4 W of total laser power being incident on the quantum diamond sensor sense this was the case for the beam sizing experiments described in Section 2.2.3. We assigned the equivalent power for each region (listed in the fourth column of Table 3) to each corresponding section as a “Heat Generation” boundary condition in SOLIDWORKS.

### 3.1.3 Simulating Thermal Boundary Conditions on a Diamond

After the creation of the Gaussian beam’s boundary conditions in the SOLIDWORKS simulation, it was necessary assign the remaining thermal boundary conditions and initial conditions to fully simulate the experimental setup. Many of these conditions are best estimates for the actual ones experienced by the quantum diamond sensor during an experiment. It is near impossible to perfectly simulate all the conditions that an object experiences in real life, but reasonable estimates for these conditions can be made, allowing us to come close to simulating the actual outcomes of the experiment. The information collected from these simulations is not exact, but it provides valuable insight into the actual thermal distribution across the quantum diamond sensor.

First, we set an initial temperature to be 294 K. This is a reasonable estimate for room temperature in the lab. The actual temperature will vary slightly from day to day.

Next, we applied a convective heat transfer coefficient of 10 W/(m$^2$·K) to all exposed faces of the diamond (i.e., all four 1 mm x 4 mm faces and one of the two 4 mm x 4 mm faces). There is no forced convection occurring across the diamond so a convection coefficient in the range of 2 W/(m$^2$·K) to 25 W/(m$^2$·K) is reasonable. The exact value for the convection coefficient is dependent on how the air is flowing in the lab over the course of an experiment. It is impossible in this scenario to perfectly determine what the convection coefficient for free air is without changing how the air is moving. Instead, we use an estimate of 10 W/(m$^2$·K). The exact outcomes from the thermal simulations might differ by a few degrees if a different convective heat transfer coefficient is used, but this change is not significant enough to be of concern.

Finally, we applied a boundary condition to the last face of the diamond to account for conductive heat loss. In the experiments, we placed the quantum diamond sensor on top of a soda-lime glass microscope slide. The slides used were Globe Scientific #1324 Glass Microscope Slides which have a thickness of 1 mm. It was assumed that the temperature of the air that the underside of the slide was exposed to remained at room temperature throughout the experiment while the backside of the diamond touching the slide was heated up. Since heat flux from conduction is dependent on difference in temperature, we derived an equation for heat flux and assigned it as the boundary condition for this face of the diamond. The general equation for heat flux $q$ is

$$q = \frac{-k\Delta T}{d} \tag{13}$$

where $k$ is the thermal conductivity of the material in W/(m$^2$·K), $\Delta T$ is the difference in temperature between the hot and cold side of the material, and $d$ is the thickness of the material. The create an equation for heat flux through the microscope slide as a function of the temperature of the temperature of the underside of the diamond, we used the following values [14]:

$$k = 1.339\ [W/(m^2 \cdot K)]$$

$$d = 1\ [mm]$$

$$\Delta T = T_{diamond} - 294\ [K]$$

Using these parameters, the following equation for heat flux through the microscope slide is generated:

$$q(T_{diamond}) = -1339(T_{diamond} - 294)\ [W/m\text{^}2] \tag{14}$$

To create the appropriate boundary condition for this face in SOLIDWORKS, we assigned a temperature dependent heat flux boundary condition defined using Equation 14. Figure 11 shows the heat flux curve generated by SOLIDWORKS using Equation 14.

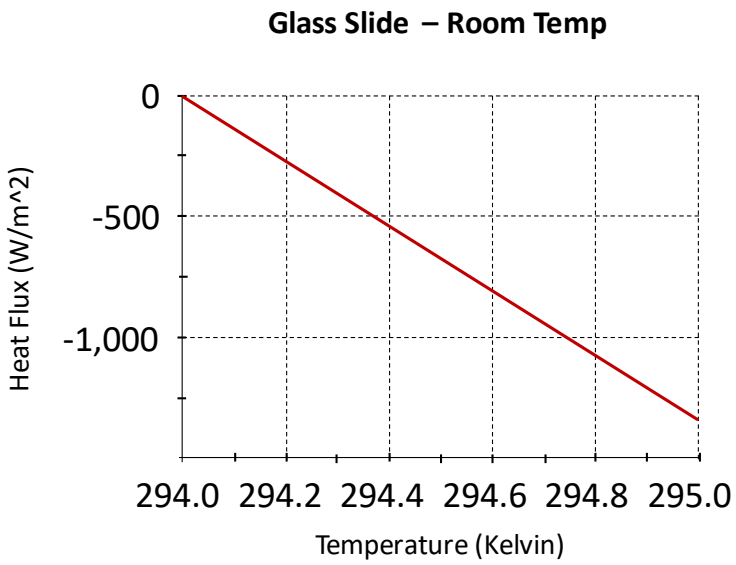


Figure 11: Heat flux curve representing heat flux through a soda lime glass microscope slide as a function of temperature.

These thermal boundary conditions and initial conditions, along with the heat generation from the Gaussian beam described in Section 3.1.2, reasonably emulate the thermal conditions experienced by the quantum diamond sensor during experiments with the Quantum Diamond Microscope. There are more boundary conditions that are less predominant and more difficult to simulate such as the heat lost due to the fluorescence from the NV centers (described in Section 1.2), or the energy lost as a result of some light from the laser beam reflecting off the diamond's surface. The impact from such phenomenon will have a slight impact on the temperature distribution across the diamond, but not so much that the simulated temperatures are not comparable or useful in understanding the thermal behavior of the system.

## 3.2 Thermal Simulations

We generated simulations in SOLIDWORKS for 2.4 W of laser power and laser beam diameters of 0.90 mm, 1.73 mm, and 2.10 mm. These laser beam diameters correspond to the three laser beam diameters used in the experiments described in Section 2.2.3. First, we adjusted the diameter of the heat distribution from the Gaussian beam accordingly for each simulation as described in Section 3.1.2. After that, we generated a mesh across the geometry of the model of the diamond, and then ran the simulations until they reached a steady state. Figure 12 shows a full picture of the simulated quantum diamond sensor after a transient thermal analysis was run on it. The beam diameter of this simulation was 0.90 mm. The resulting thermal distribution map shows a maximum temperature of 124.2 °C and a minimum temperature of 123.4 °C.

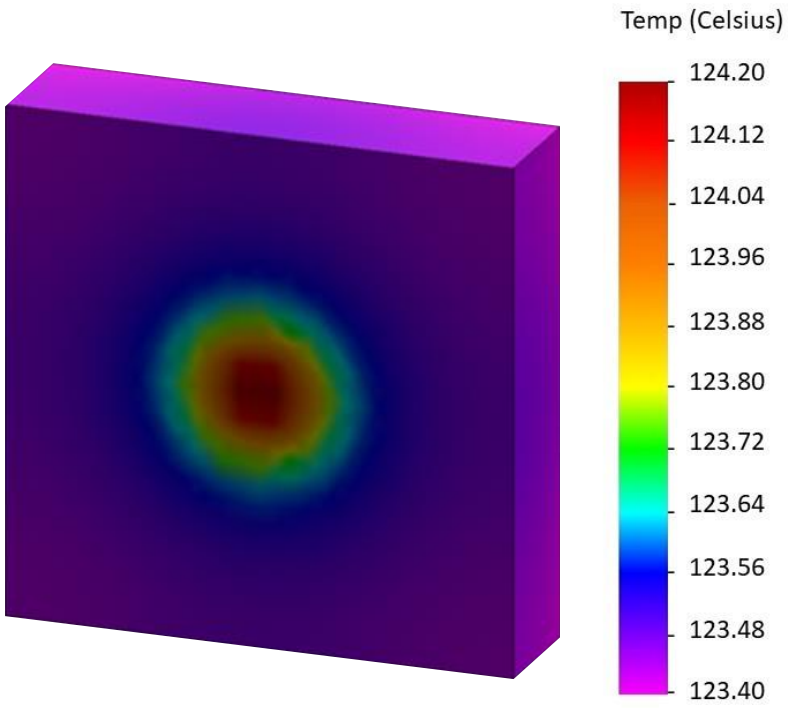


Figure 12: Full view of simulated 0.90 mm laser beam at 2.4 W of power.

To best compare the simulations with the thermal distribution maps generated from the beam sizing experiments in Section 2.2.3, it is necessary to adjust the field of view on the simulations to match field of view used in the experiments. Figure 13 shows the zoomed-in fields of view for simulations of the 0.90 mm, 1.73 mm, and 2.10 mm beams with 2.4 W of laser power.

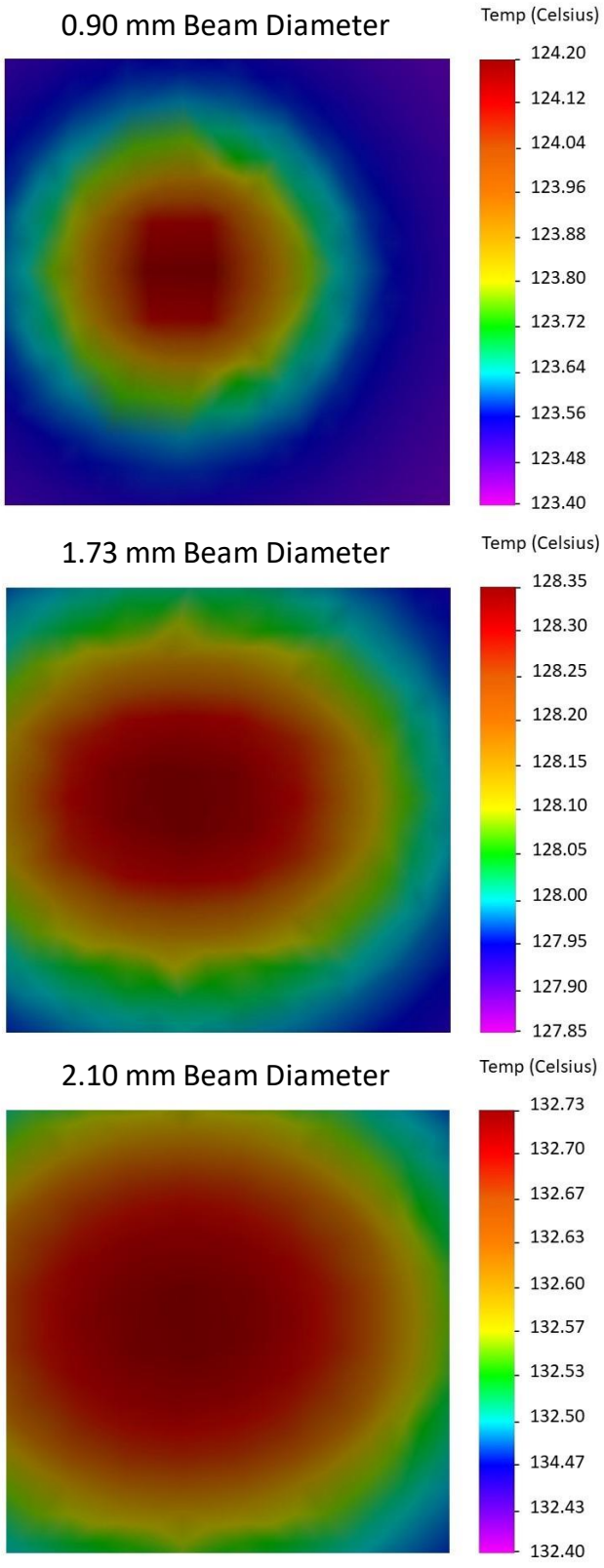


Figure 13: Simulated temperature maps of a 2 mm x 2 mm region of a diamond laser beam being hit by 0.90 mm (top), 1.73 mm (middle), and 2.10 mm (bottom) laser beam at 2.4 W of power.

For the simulation of the 0.90 mm laser beam, the maximum temperature is 124.20 °C. When compared to the thermal map for the 0.90 mm beam experiment shown in Figure 8, the maximum temperature of the simulation is approximately 2 °C lower. The lowest temperature shown in this region of the simulation is 123.48 °C. This is approximately 2.5 °C higher than the lowest temperature measured by the QDM. In the experiment, temperatures were mostly concentrated around the highest or lowest measured values. It appears that in the simulation of the 0.90 mm beam, the energy from the laser was more evenly distributed than it was in the experiment; the area between the point with the highest temperature and the point with the lowest temperature has a more continuous distribution.

For the simulation of the 1.73 mm laser beam, the maximum temperature is 128.35 °C. When compared to the thermal map for the 1.73 mm beam experiment shown in Figure 8, the maximum temperature of the simulation is approximately 0.4 °C higher. The lowest temperature shown in this region of the simulation is 127.92 °C which is approximately 3 °C higher than what we measured using the QDM. Like the experimental measurements, the distribution of temperature for the 1.73 mm beam diameter is more evenly distributed than it was for the 0.90 mm beam diameter.

For the simulation of the 2.10 mm laser beam, the maximum temperature is 132.73 °C. When compared to the thermal map for the 2.10 mm beam experiment shown in Figure 8, the maximum temperature of the simulation is approximately 1 °C lower. The lowest temperature shown in this region of the simulation is 134.47 °C which is approximately 5.4 °C higher than what was measured by the QDM. The overall distribution of temperature for the simulation of the 2.10 mm beam diameter is very continuous and fairly evenly distributed across the surface of the diamond like it was in the experimental measurements.

All values for temperature from these simulations lie within 5.4 °C of the experimental results from Section 2.2.3. The maximum temperature was more accurately simulated than the minimum temperature since all values for maximum temperature were within 2 °C of their corresponding experimentally measured temperatures. The overall range of temperatures in each simulation was less than what we observed in each of the measurements from the QDM. For the 0.90 mm beam, the simulation showed a range of approximately 1 °C where the measurement with the QDM showed a range of approximately 5 °C. For the 1.73 mm beam and 2.10 mm beam, the simulation showed a range of approximately 0.5 °C and 0.3 °C respectively while there was a range of approximately 3 °C for both of these beam diameters in the measurements made with the QDM. This could be in part due to the noise in measurements with the QDM that is not present in a simulation. Additionally, the overall higher minimum temperatures in the simulation could indicate a need to use a slightly higher convection coefficient for the surface of the diamond.

These simulations prove that this method of simulating the temperature of the quantum diamond sensor provides reasonable representations of the actual temperature distributions that result from measurements with a QDM. The fact that all of these simulations are within 5 °C of

the experimental results shows that these simulations are acceptably accurate. Additionally, because the simulated thermal boundary conditions and initial conditions are only best estimates of the actual thermal boundary conditions and initial conditions actually acting upon the quantum diamond sensor, any simulation giving temperatures within a range of $\pm 10$ °C would provide confidence that the simulations of the measurements taken using the QDM are reasonable.

# 4. Conclusions and Recommendations

This work focused on the application of the temperature measurement capabilities of the Quantum Diamond Microscope to understand the thermal behavior of the quantum diamond sensor using various parameters of measurement including laser power and laser beam diameter. This allows us to have a better understanding of what temperature samples will be subjected to while they are being measured with the QDM. This knowledge can serve as a starting point for developing methods to further dissipate heat to be able to safely image samples that are sensitive to heat or may have their properties altered due to exposure to high temperatures.

We created program for measuring temperature using the ODMR spectrum generated by a QDM with the ability to measure the average temperature in the microscope's field of view as well as generate images of the temperature distribution. This program was then successfully used to determine the effect that laser power has on the maximum average temperature reached by the quantum diamond sensor. We found that laser power and the average temperature of the diamond follow a linear relationship characterized by the equation $T(P) = 43.8 \cdot P + 26.3$ where $T$ is the temperature in degrees Celsius and $P$ is the set laser power in Watts. Following these measurements, we then used the QDM to determine the time required for the quantum diamond sensor to reach thermal equilibrium after it is first subjected to the laser beam set to various laser powers. Experiments showed that the time needed for thermal equilibrium to be reached is inversely proportional to the laser power cubed. To ensure the accuracy of measurements taken with 1.0 W of laser power, it is advised to wait up to 2 hours following the beam first hitting the diamond, while measurements taken with 4.0 W of power only need to be delayed by 4 minutes. To understand the thermal behavior of the quantum diamond sensor under exposure to different laser beam diameters, we conducted experiments to generate images of the temperature distributions across the diamond. A 166.7% increase in beam diameter resulted in a 3.2% increase in the maximum measured temperature. Additionally, we found that noise in measurements increases significantly in regions where the laser beam is not directly hitting the quantum diamond sensor, while in the regions where the laser beam is directly hitting the diamond, a higher concentration of laser power greatly reduces the noise in measurements.

Following the experimentation with the QDM, we created a method for simulating the experimental conditions that the quantum diamond sensor is exposed to during measurements using SOLIDWORKS Transient Thermal Analysis software. We calculated the thermal initial conditions and boundary conditions of the diamond and recreated them using the simulation software. All simulated temperatures measured for all laser beam diameters were within 5 °C of the corresponding temperatures measured using the QDM. While the simulated minimum temperatures were generally higher than the minimum temperatures measured with the QDM, the maximum simulated temperatures were all within 2 °C of the maximum temperatures measured with the QDM. This deviation of 2 °C is smaller than the actual deviation in the temperatures

measured using the QDM. This verifies that we can use this method for simulating the quantum diamond sensor to test new experimental setups to provide insight into the expected thermal behavior.

This work could be continued by using the simulation setup to test the effectiveness of mount designs to aid in dissipating heat from the quantum diamond sensor to further reduce the thermal loads samples are exposed to. Multiple mount designs could be modeled using SOLIDWORKS, and multiple materials could be tested. Materials that are non-magnetic, such as silicon carbide, are necessary for the manufacturing of a mount for the quantum diamond sensor in a QDM so as not to interfere with the measurements. Additionally, it is understood that the microwave loop contributes slightly to the heating of the quantum diamond sensor. Further testing of the thermal behavior of the quantum diamond sensor could be done to quantify the effect that heating from the microwave loop has on the sensor.

# References


[1] Phan, L. M. (2013). *Magnetic Field Sensing with Nitrogen-Vacancy Color Centers in Diamond* [PhD Thesis]. Harvard University.

[2] Levine, E., Turner, M., Kehayias, P., Hart, C., Langellier, N., Trubko, R., Glenn, D., Fu, R. & Walsworth, R. (2019). Principles and techniques of the quantum diamond microscope. *Nanophotonics*, *8*(11), 1945-1973. https://doi.org/10.1515/nanoph-2019-0209

[3] Glenn, D. R., Lee, K., Park, H., Weissleder, R., Yacoby, A., Lukin, M. D., Lee, H., Walsworth, R. L., & Connolly, C. B. (2015). Single-cell magnetic imaging using a quantum diamond microscope. *Nature methods*, *12*(8), 736–738. https://doi.org/10.1038/nmeth.3449

[4] Fu, R. R., Hess, K., Jaqueto, P., Novello, V. F., Kukla, T., Trindade, R. I. F., Stríkis, N. M., Cruz, F. W., & Ben Dor, O. (2021). High-Resolution Environmental Magnetism Using the Quantum Diamond Microscope (QDM): Application to a Tropical Speleothem. *Frontiers in Earth Science*, *8*. https://doi.org/10.3389/feart.2020.604505

[5] Poggioli Pardo, F. (2021). *Construction and Characterization of a Quantum Diamond Microscope.* : Worcester Polytechnic Institute.

[6] Luo, T., Lindner, L., Langer, J., Cimalla, V., Vidal, X., Hahl, F., Schreyvogel, C., Onoda, S., Ishii, S., & Ohshima, T. (2022). Creation of nitrogen-vacancy centers in chemical vapor deposition diamond for sensing applications. *New Journal of Physics*, *24*. https://doi.org/10.1088/1367-2630/ac58b6

[7] Batalov, A., Jacques, V., Kaiser, F., Siyushev, P., Neumann, P., Rogers, L. J., McMurtrie, R. L., Manson, N. B., Jelezko, F., & Wrachtrup, J. (2009). Low temperature studies of the excited-state structure of negatively charged nitrogen-vacancy color centers in diamond. *Physics Review Letters*, *102*(19), 195506. https://doi.org/10.1103/PhysRevLett.102.195506

[8] Goldman, M. L., Doherty, M. W., Sipahigil, A., Yao, N. Y., Bennett, S. D., Manson, N. B., Kubanek, A., & Lukin, M. D. (2015). State-selective intersystem crossing in nitrogen-vacancy centers. *Physical Review B*, *91*(16), 165201. https://doi.org/10.1103/PhysRevB.91.165201

[9] Barry, J., Schlossy, J., Bauch, E., Turner, M., Hart, C., Pham, L., & Walsworth, R. (2020). Sensitivity optimization for NV-diamond magnetometry. *Reviews of Modern Physics*, *92*(1). https://doi.org/10.1103/RevModPhys.92.015004

[10] Chen, Y., Li, Z., Guo, H., Wu, D., & Tang, J. (2021). Simultaneous imaging of magnetic field and temperature using a wide-field quantum diamond microscope. *EPJ Quantum Technology*, *8*. https://doi.org/10.1140/epjqt/s40507-021-00097-9

[11] NIST Office of Data and Informatics. (2022). *NIST Chemistry Webbook, SRD 69*. NIST Chemistry WebBook. https://doi.org/10.18434/T4D303

[12] *Ansys Fluent* (Ansys 2021 R2). (2021). [Computer software]. Ansys Inc.

[13] Edmund Optics Worldwide. (n.d.). *Gaussian Beam Propagation*. Edmund Optics Worldwide. Retrieved April 30, 2022, from https://www.edmundoptics.com/knowledge-center/application-notes/lasers/gaussian-beam-propagation/

[14] Thermtest Inc. (n.d.). *Materials Thermal Properties Database*. Thermtest Inc. Retrieved April 10, 2022, from https://thermtest.com/materials-database-popup/